

## RESEARCH ARTICLE

10.1002/2017JB015021

## Key Points:

- We identify the first confirmation of terrestrial crustal faults on southern Vancouver Island using high-precision earthquake relocation
- Relocated seismicity and clustering analysis provide evidence for an ~10 km thick, steeply NNE dipping fault zone that bifurcates to the east
- Subvertical secondary structures exhibit right-lateral motion and may overprint preexisting structural fabric

## Supporting Information:

- Supporting Information S1
- Data Set S1

## Correspondence to:

G. Li,  
ge.li2@mail.mcgill.ca

## Citation:

Li, G., Liu, Y., Regalla, C., & Morell, K. D. (2018). Seismicity relocation and fault structure near the Leech River fault zone, southern Vancouver Island. *Journal of Geophysical Research: Solid Earth*, 123, 2841–2855. <https://doi.org/10.1002/2017JB015021>

Received 26 SEP 2017

Accepted 3 MAR 2018

Accepted article online 12 MAR 2018

Published online 13 APR 2018

## Seismicity Relocation and Fault Structure Near the Leech River Fault Zone, Southern Vancouver Island

Ge Li<sup>1</sup> , Yajing Liu<sup>1</sup> , Christine Regalla<sup>2</sup> , and Kristin D. Morell<sup>3,4</sup> 
<sup>1</sup>Department of Earth and Planetary Sciences, McGill University, Montréal, Québec, Canada, <sup>2</sup>Department of Earth and Environment, Boston University, Boston, MA, USA, <sup>3</sup>School of Earth and Ocean Sciences, University of Victoria, Victoria, British Columbia, Canada, <sup>4</sup>Department of Earth Sciences, University of California, Santa Barbara, CA, USA

**Abstract** Relatively low rates of seismicity and fault loading have made it challenging to correlate microseismicity to mapped surface faults on the forearc of southern Vancouver Island. Here we use precise relocations of microseismicity integrated with existing geologic data to present the first identification of subsurface seismogenic structures associated with the Leech River fault zone on southern Vancouver Island. We used the HypoDD double-difference relocation method to relocate 1,253 earthquakes reported by the Canadian National Seismograph Network catalog from 1992 to 2015. Our results reveal an ~8–10 km wide, NNE dipping zone of seismicity representing a subsurface structure along the eastern 30 km of the terrestrial Leech River fault zone and extending 20 km farther eastward offshore, where the fault bifurcates beneath the Juan de Fuca Strait. Using a clustering analysis, we identify secondary structures within the NNE dipping fault zone, many of which are subvertical and exhibit right-lateral strike-slip focal mechanisms. We suggest that the arrangement of these near-vertical dextral secondary structures within a more general NE dipping fault zone, located 10–15 km beneath the Leech River fault as imaged by LITHOPROBE, may be a consequence of the reactivation of this fault system as a right-lateral structure in crust with a preexisting NNE dipping structural fabric. Our results provide the first confirmation of active terrestrial crustal faults on Vancouver Island using a relocation method. We suggest that slowly slipping active crustal faults, especially in regions with preexisting foliations, may result in microseismicity along fracture arrays rather than along single planar structures.

## 1. Introduction

Crustal fault systems can exhibit relatively slow loading rates and long recurrence intervals and may be characterized by poorly connected fault arrays and fracture networks (Asano & Iwata, 2016; Ferranti et al., 2014). Structural complexities and low rates of microseismicity can present challenges to characterizing the subsurface geometry, kinematics, and seismic potential of crustal fault systems in low strain rate regimes. Crustal faults with relatively slow slip rates ( $< \sim 1$  mm/yr) are nonetheless capable of producing damaging, surface-rupturing earthquakes such as the 2016 Mw7.1 Kumamoto earthquake, which ruptured the Futagawa-Hinagu fault system in central Kyushu, Japan (Asano & Iwata, 2016). Despite an average horizontal slip rate of only ~0.88 mm/yr in the late Quaternary (Tsutsumi & Okada, 1996), this fault system produced a maximum coseismic slip of ~5.1 m (Asano & Iwata, 2016) and caused at least 50 casualties and ~3,000 injuries.

The challenges presented by regions with relatively low strain rates have been especially realized in the forearc of northern Cascadia on southern Vancouver Island. Historical records and seismicity monitoring suggest that seismogenic crustal faults on Vancouver Island contribute to active strain accumulation in northern Cascadia (Balfour et al., 2012; Cassidy & Waldhauser, 2003) and may have hosted large crustal earthquakes in 1918 (M 7.0) and 1946 (M 7.3) (Rogers, 1994). Moreover, GPS studies show that a component of the regional geodetic strain field is accommodated by low strain rates of 20–30 nanostrain per year ( $10^{-9}$  year<sup>-1</sup>) (McCaffrey et al., 2007), along a network of active faults within Washington (Johnson et al., 1999) and Oregon (Sherrrod et al., 2008, 2016), and beneath the Strait of Georgia (Mosher et al., 2000). Despite the evidence for crustal seismicity in the southern Vancouver Island area (Rogers, 1994), it has proven difficult to correlate microseismicity to mapped surface faults (Cassidy et al., 2000; Mosher et al., 2000), and the geometry and kinematics of potentially seismogenic crustal faults remain poorly constrained.

Here we utilize new, precise relocations of microseismicity, integrated with existing geologic observations, to investigate the activity of Leech River fault zone (LRFZ), one of the most prominent fault systems in the

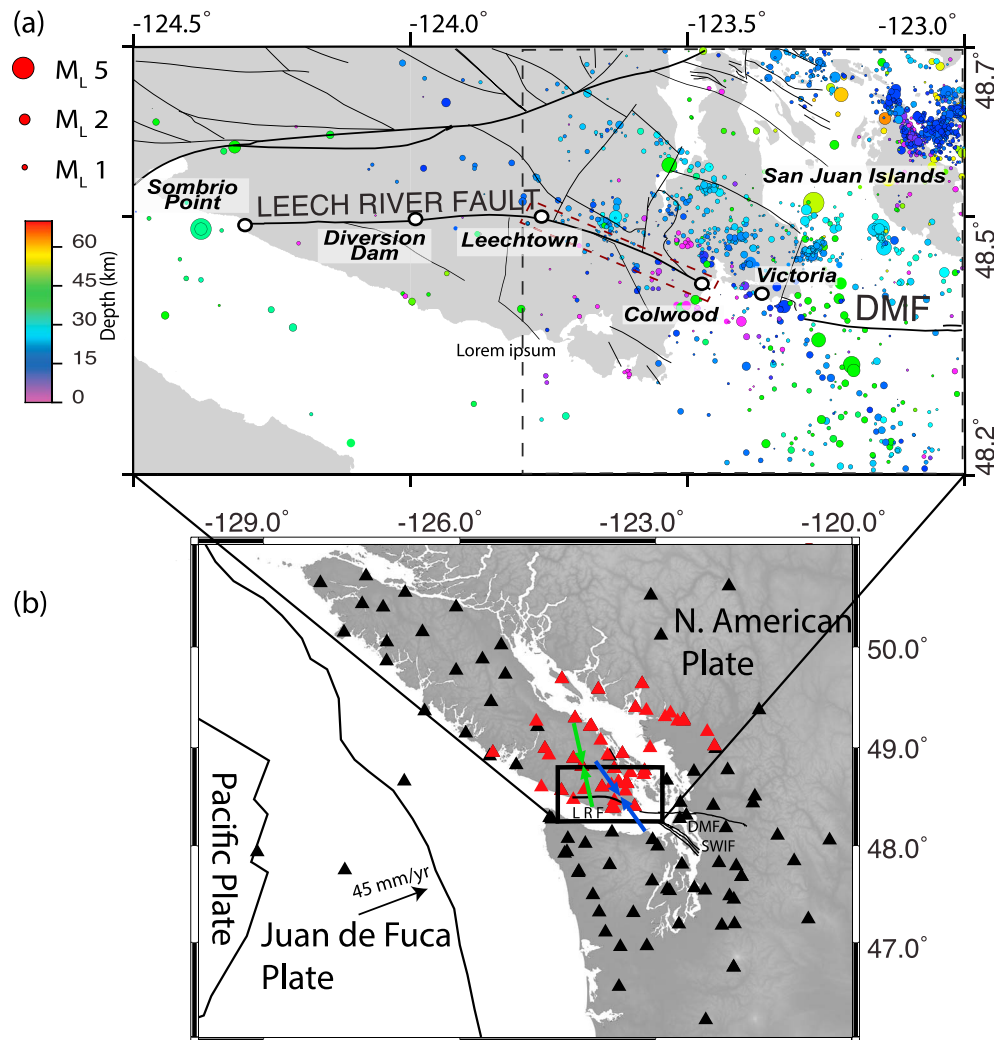


**Figure 1.** (a) Map of the study area showing locations of Canadian National Seismographic Network cataloged earthquakes from 1992 to 2015,  $M_L$  0.1 to 4.9 and depth  $< 60$  km, and mapped faults in British Columbia (after Massey et al., 2005). Black dashed-line box represents our study area, as in Figures 4 and 5. Brown dashed-line box represents the region of the geological survey by Morell et al. (2017). (b) Triangles denote the location of stations used for catalog phase arrivals (Red: phase arrivals from manual picks and waveform cross-correlation). Two maximum horizontal compression orientations inverted from earthquake focal mechanisms are also shown,  $S_{Hmax1}$  in green and  $S_{Hmax2}$  in blue (Balfour et al., 2011). LRF: Leech River fault; DMF: Devil's Mountain Fault; SWIF: Southern Whidbey Island fault.

southern portion of Vancouver Island, which extends for  $\sim 60$  km along strike (Figure 1). The LRFZ juxtaposes basalts of the Metchosin Formation of the Crescent Terrane to the south against the Leech River Complex of the Pacific Rim Terrane to the north (Clowes et al., 1987; MacLeod et al., 1977) and is thought to have initially formed during the accretion of the Crescent Terrane to western North America (e.g., Massey et al., 2005; Rushmore & Cowan, 1985). This fault has been classically interpreted as inactive since the Eocene (MacLeod et al., 1977). However, recent field and light detection and ranging evidence reveal subparallel, steeply dipping topographic features that suggest late Quaternary activity on this fault (Morell et al., 2017). Channels and Quaternary colluvium offset by 2 to 4 m suggest that at least two  $M$  6–7 earthquakes have occurred along the LRF since  $\sim 15,000$  years ago. Seismicity lineations and streaks related to subsurface structures or to mapped surface fault expressions have been previously recognized on nearby fault systems in the Strait of Georgia (Cassidy et al., 2000) and San Juan Island area (Balfour et al., 2012) offshore. Active structures have also been identified within the Strait of Juan de Fuca (Barrie & Greene, 2015, 2018). However, due to the relatively low seismicity rate and slow loading rate in this region, microseismicity has yet to be directly associated with mapped terrestrial surface faults, and the subsurface geometries of potentially seismogenic crustal structures are poorly constrained. Given its along-strike length and proximity to Victoria, the provincial

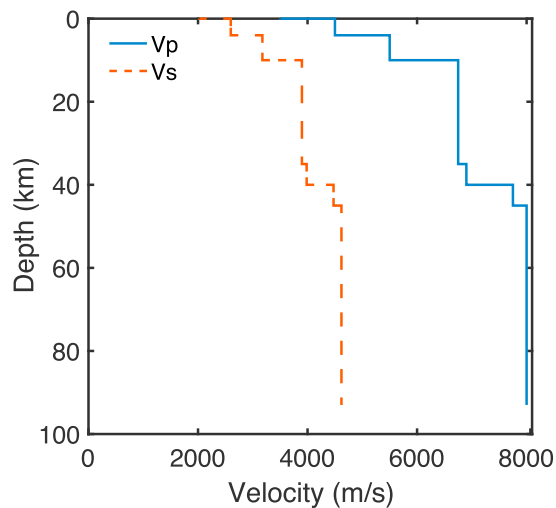


**Figure 2.** One-dimensional velocity model used in HypoDD relocation.  $V_p$  is obtained based on Fisher et al. (1999) and Ramachandran et al. (2006). The  $S$  wave velocity  $V_s$  is calculated by assuming a constant ratio of  $V_p/V_s = \sqrt{3}$ .

capital of British Columbia, the seismogenic potential of the LRFZ is also a key issue for local seismic hazard assessment (Zaleski, 2014).

In this paper, we use a double-difference earthquake relocation algorithm (HypoDD) to relocate 1,253 earthquakes reported by the Canadian National Seismographic Network (CNSN) near the LRFZ between 1992 and 2015 and interpret the source properties of these crustal earthquakes in the context of regional geology. Relocated earthquakes are further analyzed using several clustering methods to identify potential seismogenic structures and their geometry. Our relocation and clustering analysis results provide seismic evidence for potentially active structures beneath southern Vancouver Island and highlight the presence of a broad ( $\sim 10$  km wide) fault zone and network of fractures that may accommodate active strain within the LRFZ.

## 2. Data and Relocation Procedure

We apply a double-difference earthquake relocation algorithm HypoDD (Waldhauser & Ellsworth, 2000) to obtain precise relative

hypocenters of 1,253 earthquakes with local magnitudes ( $M_L$ ) ranging from 0.1 to 4.9, reported by the CNSN catalog between January 1992 and March 2015 within the LRFZ study area (events within the black box in Figure 1b). Earthquakes before 1992 (275 in total) were not used in the pre-processing step due to the lack of sufficient arrivals. We use a 1-D velocity model (Figure 2) derived from the  $P$  wave model of the northern Cascadia forearc region using both active and passive seismic data on southwestern British Columbia and northwestern Washington (Fisher et al., 1999; Ramachandran et al., 2006). This velocity model has better quality at shallower depths of 0–30 km, which approximately correlates to the thickness of forearc crust ( $\sim < 30$  km), than the model at deeper regions. This resolution is indicated by better checkerboard test results, denser seismic ray hits and higher semblance values at depths of 0–30 km (Ramachandran et al., 2006).

We combined differential traveltimes determined from the following two separate sources: (1)  $P$  wave and  $S$  wave arrivals provided by the CNSN catalog at 169 seismic stations (triangles in Figure 1b (Quality A, pick uncertainty is  $\pm 0.25$  s, as reported by CNSN analyst)). For each event pair, only phases recorded by stations within 200 km from the event pair were used; (2) differential traveltimes for  $P$  waves were determined from waveform cross-correlation for events with a hypocentral separation less than 10 km and with a cutoff correlation coefficient of 0.8. The waveforms used for cross-correlation were based on a 3 s long window centered at the  $P$  arrival. Waveforms were filtered using a 1–10 Hz Butterworth filter before correlation. Only the vertical component was used for  $P$  wave arrivals. Eighty-two percent of the differential time shift due to cross-correlation is within 0.25 s, as shown in Figure 3a. The full data set used for relocation consisted of (1) 1,417,630 cross-correlation differential times and (2) 91,505  $P$  wave and 82,752  $S$  wave differential times based on CNSN catalog reported arrivals. In total, there were 1,591,887 differential times used in the relocation.

To verify the quality of the catalog arrival times, we also manually picked  $P$  arrivals (2,179 in total) using waveform data from 50 stations (red triangles in Figure 1b), following a two-step procedure. First, we determined the  $P$  phase onset time from waveform data based on a maximum kurtosis and  $\kappa$  statistics method (Saragiotis et al., 2004; Yu et al., 2016) with a sliding time detection window. Kurtosis is a measure of whether the data are peaked or flat relative to a statistical normal distribution; the kurtosis of a standard normal distribution is theoretically zero. Therefore, we can discriminate the  $P$  phases under the assumption that, unlike background noises, the  $P$  phases do not follow the Gaussian distribution. Second, we visually checked the waveform recordings to remove outliers and constrain the reliability of the autodetermined  $P$  onsets. A comparison between manually picked  $P$  wave arrivals and those provided by CNSN catalog shows that  $\sim 95\%$  (2,076/2,179) of the traveltime differences are smaller than 0.25 s (Figure 3a). These traveltime differences are consistent with the data quality reported by CNSN. The results presented in the following section are relocations using catalog and cross-correlation combined traveltime differences.

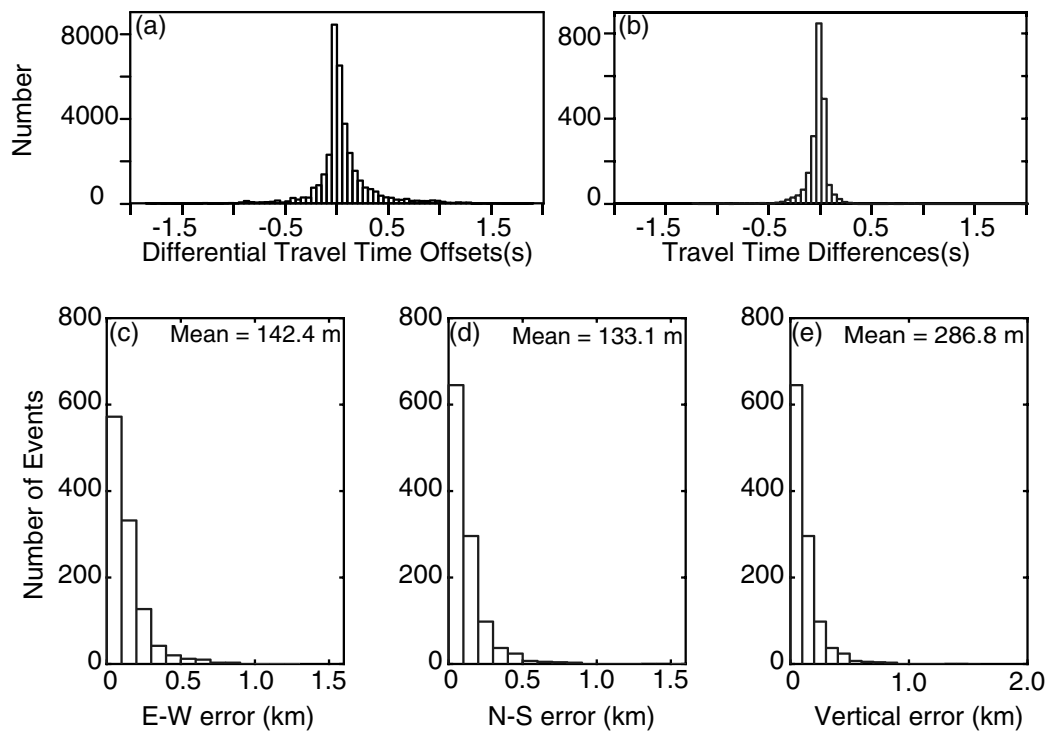


**Figure 3.** (a) Differences between catalog and cross-correlation differential times. (b) Traveltime differences between manually picked and catalog reported *P* wave arrivals. (c–e) Relocation errors estimated by bootstrapping for the entire catalog.

Key HypoDD parameters are listed in Table 1. Their values are chosen in order to optimize the quality of phase pairs and event connectivity. We also ran relocation trials by varying MAXDIST (maximum distance allowed between the centroid of each event pair and stations) between 50 km and 200 km. The optimal value of MAXDIST is considered to have both a small traveltime residual and a minimum number of weak event pairs. We found that among the tested values, a MAXDIST of 100 km was the optimal choice, which yielded a traveltime residual of 0.0149 ms and a percentage of weak pairs of 12%. We considered other values not ideal as traveltime residuals over 23 ms were obtained for MAXDIST values of 150 km and 200 km and 37% of weak pairs were obtained for 50 km. Hypocenters located above the ground were also removed. In total, we relocated 1,126 out of the original 1,253 events at a recovery rate of ~ 90%.

Given the large data set, we used the least squares conjugate gradients method in our relocations (Paige & Saunders, 1982). Because the least squares conjugate gradients method solves the damped least squares problem, we set the damping value ( $\lambda$ ) to 70, in order to stabilize the system with a reasonable utilization percentage (~80%) of observation data and data residual (21 ms). A systematic test and search for the optimal damping value are presented in supporting information Figure S2. Relocation uncertainties for the entire catalog were estimated statistically using a bootstrap method, which yielded a cluster of 100 location points for each event, displaying “location vibrations” due to traveltime perturbations. Relocation uncertainties are thus defined as the standard error in each dimension (northing, easting, and vertical). The resulting average bootstrapping errors for this relocation procedure are about 142 m, 133 m, and 286 m in east, north, and vertical directions, respectively (Figures 3c–3e). It should be noted that, unlike relocation studies in California (e.g., Waldhauser & Schaff, 2008, in Northern California and Hauksson & Shearer, 2005, in Southern California), the inclusion of cross-correlation-determined traveltime differences does not have a significant effect on the final relocation results in this study area. Relocated earthquake positions differ by only 500–1000 m. The general patterns of seismicity relocated with and without the cross-correlation differential times are similar in this region and would not change the overall interpretations presented in this paper. This minimal difference in relocation results has also been observed in seismicity relocation studies in the Charlevoix Seismic Zone, eastern Canada, for example, by Yu et al. (2016). Although *S* wave differential times obtained from

**Table 1**  
Key hypoDD Parameters Used in the Relocation

Parameters	Values
MAXNGH <sup>a</sup>	8
MAXSEP <sup>b</sup>	10 km
MINLINK <sup>c</sup>	8
MAXDIST <sup>d</sup>	100 km
Catalog <i>P/S</i> arrival weight ratio	1/0.5 (first 5 iterations) 0.01/0.005 (next 15 iterations)
Cross-correlation <i>P/S</i> arrival weight ratio	0.01/0.005 (first 5 iterations) 1/0.5 (next 15 iterations)
Damping term $\lambda$	70

<sup>a</sup>MAXNGH: Maximum number of neighbor events. <sup>b</sup>MAXSEP: Maximum distance allowed between the centroid of each event pair and stations. <sup>c</sup>MINLINK: Minimum number of phase pair links. <sup>d</sup>MAXDIST: Maximum distance allowed between the centroid of each event pair and stations.

cross-correlation were not included in our study, we consider that this will not significantly influence the relocation results.

### 3. Relocation Results

The results of the HypoDD relocations show two regions of seismicity in map view, one near the San Juan Island area, and one beneath the surface trace of the Leech River fault (LRF) and its offshore extension (Figure 1). In depth cross-sectional view, earthquakes in this area can be divided into upper continental seismicity (depth < 30 km) and underlying subduction slab seismicity, separated by a ~10 km gap (Figure 4). This seismicity gap coincides with a highly reflective zone bounded by what are generally termed E-reflectors (marked as E1 and E2 for the top and bottom reflectors respectively in Figure 4) imaged in the LITHOPROBE project (Clowes et al., 1987). We will discuss the seismicity gap and deeper events in the context of the reflection zone interpretation and relation to the Cascadia subduction slab in section 5. We focus on the 470 relocated events in our study area, with depth < 30 km, in order to investigate potential crustal fault structures in the overriding plate in the vicinity of the LRFZ.

To a first order, crustal earthquakes associated with the LRFZ reveal a broad (~10 km wide) zone of seismicity at depths of 15–30 km that extends for ~ 30 km along the terrestrial mapped fault trace and an additional

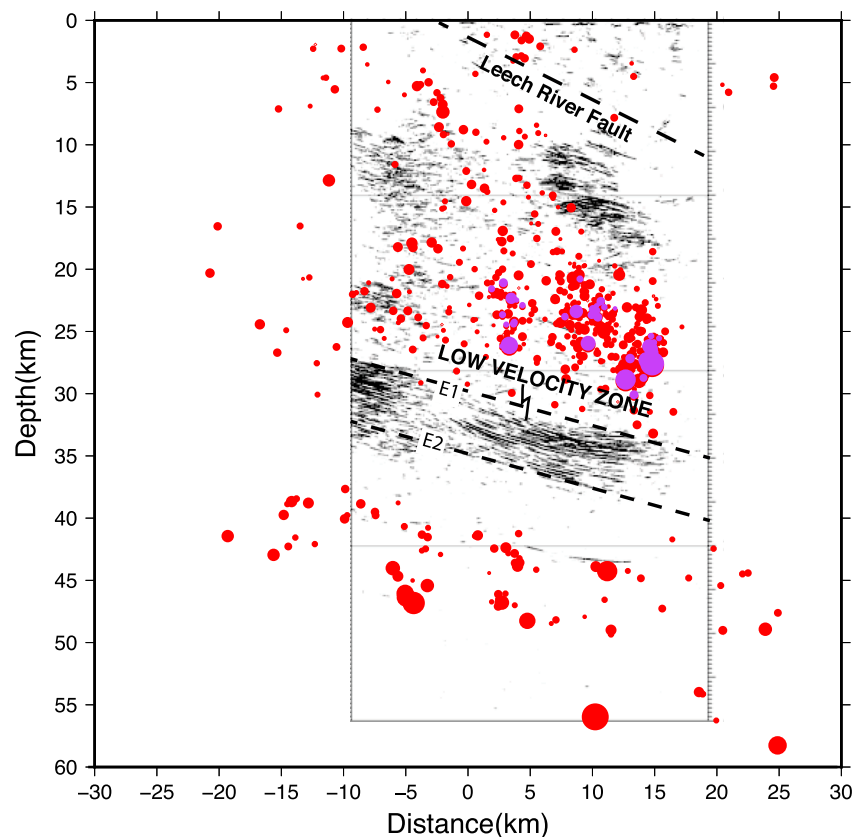


**Figure 4.** Comparison of relocated seismicity (this study) and crustal structure determined from LITHOPROBE seismic reflection Line 02 (Clowes et al., 1987). See Figure 5 for line locations. Relocated earthquakes (crustal earthquakes and deeper earthquakes) within the black dashed box in Figure 1 are projected along profile P1-P1', approximately perpendicular to the Leech River fault. Earthquakes in the San Juan Islands region are excluded. Purple dots represent repeating events in Figure 5a. Thick dashed line above 10 km denotes the LITHOPROBE-inferred Leech River fault as the geological terrane boundary. E1 and E2 denote the top and bottom reflectors of the inferred high reflection zone (also termed low-velocity zone), respectively.



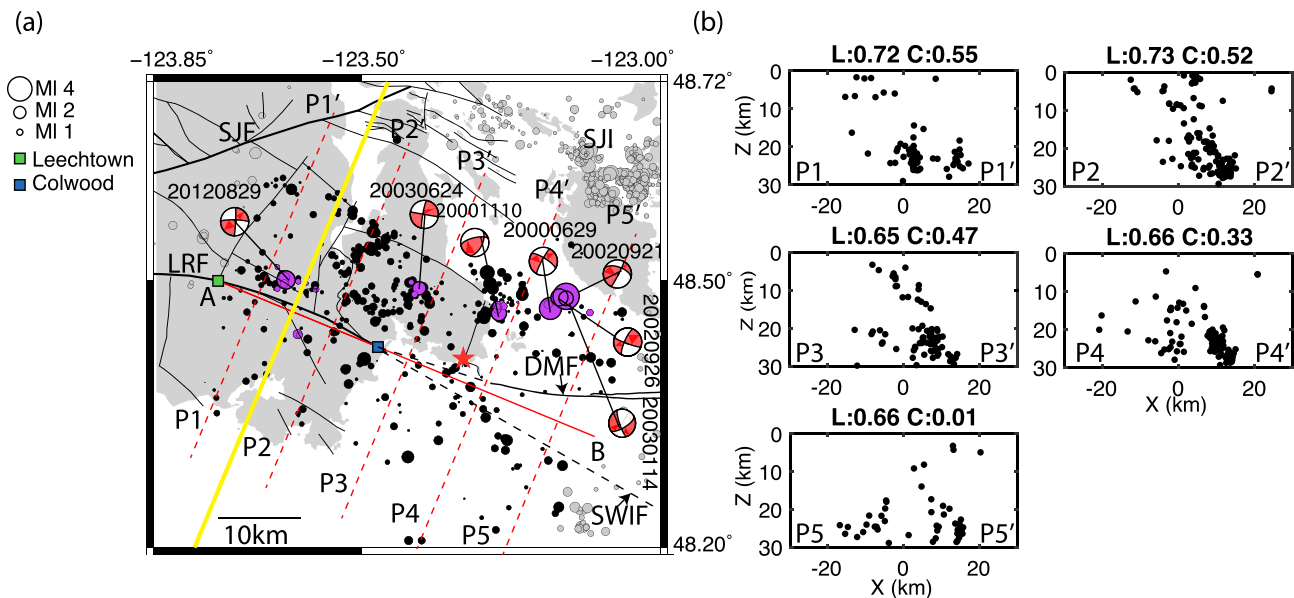


**Figure 5.** (a) Relocated crustal earthquakes, that is, depths <30 km. Black and purple (repeating events, some with focal mechanism solutions) dots represent earthquakes analyzed in (b). Gray dots represent background seismicity. The yellow line represents reflection profile LITHOPROBE Line 02. Red dashed lines P1-P1' to P5-P5' represent cross sections shown in the following sections. Red solid line (A-B) connecting the Leechtown and Colwood is the “zero x-position line” of P1-P1' to P5-P5'. The black dashed line represents the proposed offshore extension of the Leech River fault (LRF) to the strike of the Southern Whidbey Island Fault (SWIF) and Devil's Mountain Fault (DMF). (b) Cross-sectional view of crustal earthquakes along profiles P1-P1' to P5-P5'. Events within 5 km distance normal to each profile are plotted.  $L$ : Linearity value;  $C$ : Correlation coefficient. SJF = San Juan Island; SJF = San Juan fault.

~20 km further to the east into the Juan de Fuca Strait (Figures 5a and 5b). We project the crustal seismicity onto five profiles (P1-P1' to P5-P5') perpendicular to the LRF surface trace between Leechtown and Colwood and its offshore extension (Figure 5a). Each depth cross section contains seismicity within 5 km on each side of the profile (Figure 5b). We define two quantitative coefficients, linearity  $L$  and correlation coefficient  $C$ , to describe the spatial pattern of seismicity on each profile. Here  $L = 1 - \frac{\lambda_2}{\lambda_1}$  ( $\lambda_1$  and  $\lambda_2$  are the maximum and minimum eigenvalues of the covariance matrix of the earthquake locations in  $(X, Z)$  coordinates:  $X$  is the distance along the profile and  $Z$  is vertical depth (Figure 5b)). Thus,  $L = 1$  indicates a line and  $L = 0$  represents a circle. The correlation coefficient  $C$  measures the linear relationship between  $X$  and  $Z$ . A potential fault highlighted by seismicity is expected to have a large  $L$  value. A dipping fault is characterized by large  $L$  and  $C$  values (Figure S3). As shown in Figure 5b, both the  $L$  and  $C$  values decrease eastward from P1-P1' to P5-P5', with a  $C$  value of nearly 0 at P5-P5'. In general, higher  $L$  and  $C$  values at P1-P1' to P3-P3' suggest that seismicity delineates a single, continuous NNE dipping structure in profiles P1-P1' to P3-P3'. From P4-P4' to P5-P5', it becomes impossible to fit the data onto a single uniformly dipping structure due to near-zero  $C$  values. On each profile, seismicity appears to delineate a network of linear structures embedded in a broad seismic zone. In order to better distinguish active structures from the background seismicity and their spatial variations along the LRF objectively and quantitatively, we apply a clustering analysis to the relocated hypocenters as described in section 4.

#### 4. Cluster Analysis and Results

To identify seismic clusters from relocated earthquakes, we first attempted to use the Nearest Neighbor Distance (NND) method (Zaliapin & Ben-Zion, 2013), a general clustering method based on the space-time-magnitude proximity between event pairs. Results obtained from the NND method suggest that seismicity in our study area is dominated by spatial clusters instead of foreshock-mainshock-aftershock sequences (see supporting information for details of NND analysis). We recognize that the NND method can be adjusted to prioritize space over differential magnitude or time. When both  $b$  value and time exponent are set to 0, the NND method can be used as a clustering method that constructs clusters solely based on the Euclidean distances between earthquake hypocenters. However, we consider this method not applicable to this study due to the following two considerations. First, the NND method lacks the ability to distinguish seismic structures

that are embedded within background seismicity, which is typical in our study area (Figure 5). Second, an earthquake cluster may consist of a certain number of events that are close in space but do not necessarily represent a meaningful seismic structure. It is therefore possible that the NND method will construct clusters that have low linearity values and correlation values, which likely do not represent meaningful seismic structures. Therefore, to identify seismic clusters in space, we performed our clustering analysis based on (1) the Gaussian Mixture Model (GMM) method, which quantifies high statistical significance in spatial locations and (2) waveform cross-correlation in search of repeating events (RE) indicative of seismic energy radiation from common sources, complemented by focal mechanism solutions. The GMM method is capable of discriminating seismic clusters from background events by maximizing the distribution likelihood function, instead of building clusters based on a distance threshold as in the NND method. In this study, we use “group” for events categorized based on the GMM method and RE analysis. In this context, if an earthquake group met certain quantitative criteria, including high linearity and correlation coefficients, and a minimum event number in each group, it was classified as a “cluster.” Only earthquake clusters were interpreted as seismic structures.

#### 4.1. GMM Analysis

The GMM method is a statistical analysis method that divides a spatial distribution of points into any given number of groups by maximizing the distribution likelihood function representing a mixture of several multivariate Gaussian Models (McLachlan & Peel, 2000). The GMM method was performed based on 2-D earthquake locations projected onto five profiles oriented approximately perpendicular the strike of the LRF. The GMM alone, however, cannot determine seismic clusters due to the following three reasons:

1. Groups generated by this method may not represent meaningful seismic clusters, as groups with small  $L$  or  $C$  values can be generated in the process. This complication requires further constraints on the cutoff values of  $L$  and  $C$  to discriminate seismic clusters from other GMM groups.
2. Meaningless small groups with few events but extremely large linearity values can be generated during the GMM procedure, especially when fitting a large number of groups. For example, a GMM group with two events always has a linearity of 1. Therefore, groups with insufficient events were treated as background seismicity regardless of their  $L$  values. In practice, it requires each group to have a minimum number of 10 events.
3. Events can be assigned into any number of groups using the GMM method. Different scenarios with different group numbers ( $k$ ) will usually lead to different clustering results. Groups determined as seismic clusters in one scenario may no longer be preserved in other scenarios. Only seismic structures that are always defined regardless of the assigned group number are retained for further analysis.

Considering these factors, starting from the P1-P1' to P5-P5' profile distributions (Figures 5b and S5), we utilized a multilevel strategy to determine seismic clusters using the GMM method. First, we divided each profile of seismicity into  $k$  GMM groups, each group consisting of a minimum of 10 events and with a linearity coefficient greater than  $L_0$ . Second, we varied  $k$  from 2 to 9 and repeat step 1. Finally, we retained stable clusters for subsequent interpretations. Several cutoff values were used in the above analysis. Using these criteria, we then defined a stable cluster as any GMM group that survived at least four clustering scenarios, which is half of a total of eight runs for  $k = 2$  to 9. In order to test the influence of  $L_0$  on cluster identification, we varied the linearity cutoff value  $L_0$  from 0.5 to 0.9. We note that different choices of  $L_0$  may result in slightly different stable clusters; for example, a stable structure that survives four runs with an  $L_0$  of 0.7 may only survive three runs (insufficient stability) when  $L_0$  is increased to 0.8. In most cases, however, the influence of  $L_0$  on the determination of stable structures can be negligible, as shown in Figure S5.

#### 4.2. Repeating Events Analysis and Focal Mechanism Solutions

To further test the robustness of the GMM-determined structures, we performed a repeating earthquake analysis to search for event pairs with highly similar waveforms, which may characterize repeated ruptures of the same source fault (Gardonio et al., 2015). Here we defined REs pairs as those closely spaced (hypocentral distance  $< 5$  km) earthquakes with waveform cross-correlation coefficients greater than 0.9 detected at  $\geq 4$  stations. The waveforms used for the cross-correlation were constrained to a 3 s long window around the  $P$  arrival. This method was performed based on 3-D earthquake locations. It should be noted that our definition here of REs is not as rigorous as in previous studies (Gardonio et al., 2015) in several aspects: (1) REs in

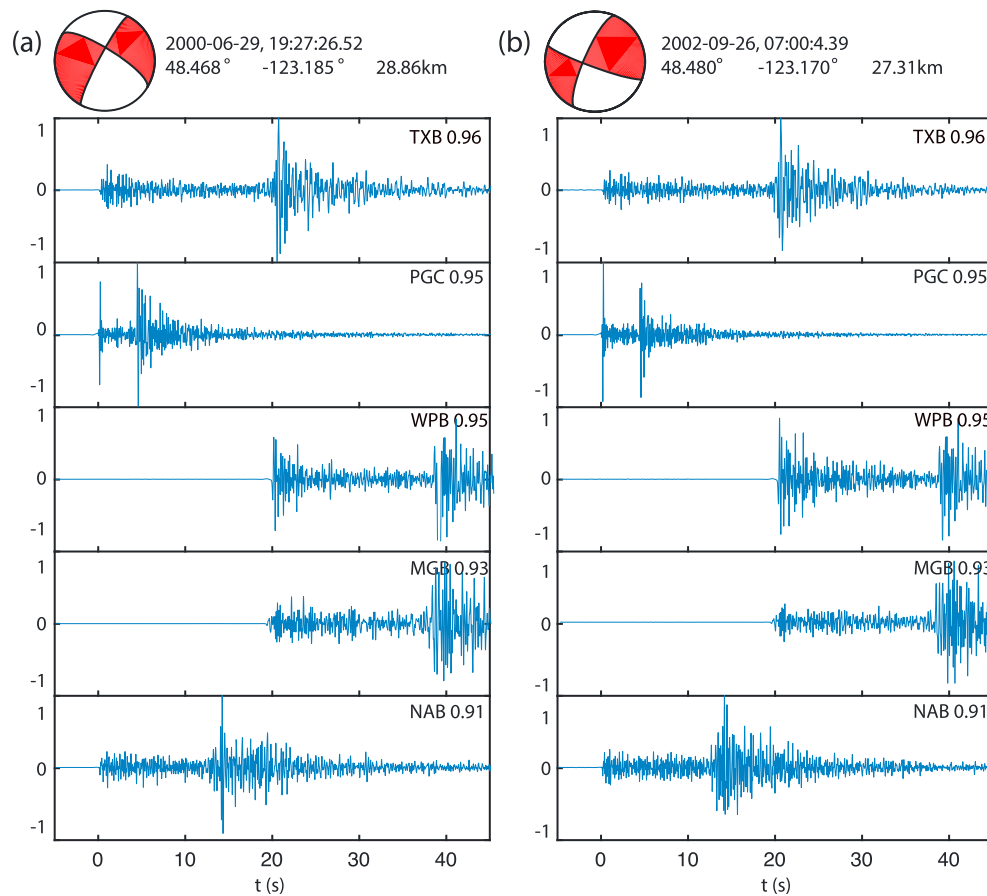


**Figure 6.** (a and b) Fault plane solutions and normalized waveforms in vertical component for a repeating event pair at five different stations. Time is aligned relative to *P* wave arrival at each station. Station names and cross-correlation coefficients are noted at the top right of each panel.

previous studies have regular occurrence intervals. No such periodicity is observed in our study. (2) Hypocentral separations in previous REs can reach as small as  $\sim 100$  m. Although a more appropriate term for the LRF REs would be “highly similar events,” we keep the term “Repeating Events” for ease of reference. RE pairs can then be grouped spatially into RE groups linked by common events (Kimura et al., 2006). This procedure results in 45 RE pairs, which constitute 10 RE groups with the largest group containing 10 events.

We also calculated focal mechanism solutions for REs with magnitudes  $>2.0$ , which can provide insights in the behavior of seismic structures. We used HASH to perform a grid search for the solution by minimizing the *P* polarity misfits on observed stations (Hardebeck & Shearer, 2003). Waveform *P* polarities were picked manually for stations within 200 km and the grid size was set to be  $5^\circ$ . Average estimated earthquake location errors of 150 m in the horizontal direction and 290 m in the vertical direction were considered for solution uncertainties. The inversion also reports estimations of fault plane uncertainties, where quality is graded from A to E. In total, we determined seven focal mechanisms with quality B assigned for all solutions, indicating the average misfit fraction is  $<0.2$ . Figure 6 shows the correlated waveforms of two representative REs and their similar focal mechanisms.

#### 4.3. Seismicity Clusters Identified From GMM and RE Methods

Figure 7 shows the final results after the clustering analysis using the GMM and RE methods. We have identified seven stable clusters using the GMM method indicative of seismic structures. These include two vertical structures located in P1-P1' (Clusters 1 and 2), two NNE dipping structures in P3-P3' (Clusters 3 and 4), an NNE dipping structure in P4-P4' (Cluster 5), and a vertical structure and a moderately SW dipping structure in P5-P5' (Cluster 7 and Cluster 6, respectively). Among the seven stable clusters, Clusters 1, 3, 5, and 7 are



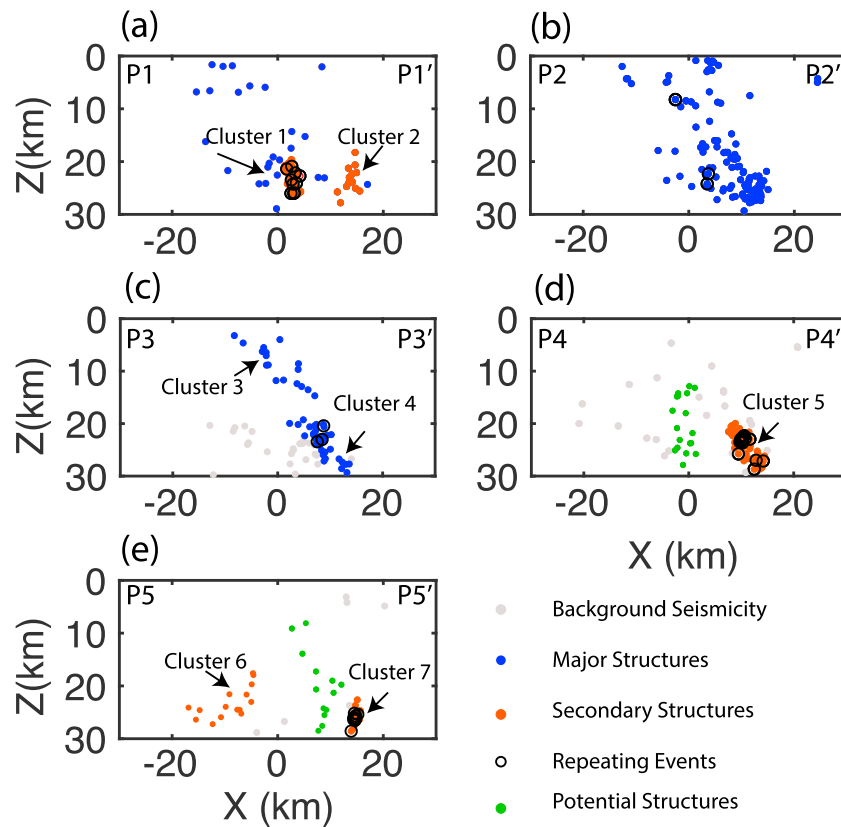


**Figure 7.** (a–e) Final results from clustering analysis. Blue dots represent seismic clusters determined by the Gaussian Mixture Model method. Gray dots represent background seismicity, that is, events not constituting a seismic cluster. Black open circles represent repeating event clusters. Brown dots represent secondary structures.

retained regardless of the choice of  $L_0$ . Clusters 2 and 4 can be determined for  $L_0 \leq 0.8$ ; Cluster 6 is determined only for  $L_0 \leq 0.6$ . We also highlight potential structures (green dots) determined by the GMM method without sufficient stabilities.

Clusters constructed using the RE method are consistent with Clusters 1, 5, and 7 identified by the GMM method (Figure 7 and Table 2). We used the conventional method of projecting seismicity on cross-section profiles perpendicular to the fault strike in order to investigate the spatial variation of crustal seismicity. We divided the region into five profiles to both keep sufficient seismicity in each profile as well as to retain the ability to identify along-strike variations. However, the RE method, which was performed based on 3-D earthquake locations, is not sensitive to the choice of 2-D profiles. We note that, while the GMM method was performed based on 2-D earthquake locations and could be sensitive to the choice of projection profile orientation and profile number, the agreement in identified clusters and indicated vertically dipping structures by these two independent methods confirms the robustness of our strategy, suggesting that clusters identified by GMM are not an artifact of the projection profile orientation. To further address this concern, we performed the GMM method with 3-D earthquake locations. As shown in supporting information Figure S6, three clusters are determined using the 3D GMM method. They correspond to Clusters 1, 5, and 7 in Figure 7, which we consider to be the most stable as they are determined by the combination of the 2-D GMM and the RE method. This 3-D GMM test confirms that the result obtained by the 2-D method is robust.

Combining the GMM and RE results, we assigned a quality classification to each of the clusters based on their stability in our multilevel selection strategy, as described in Table 2.

The results of the GMM and RE cluster analysis allow us to define primary seismogenic structures and assess how their geometry varies from P1–P1' to P5–P5' (Figure 7). Seismicity in profiles P1–P1' and P2–P2' shows an NNE dipping structure. In profile P3–P3', we identified two stable clusters 3 and 4, which broadly define a

**Table 2**  
Quality Classification<sup>a</sup> (A–D) Assigned to Clusters Identified

Cluster ID	Linearity (L)	Correlation (C)	Number of events <sup>b</sup>	Repeating events <sup>c</sup>	Quality
1	0.91	0.54	37	Yes	A
2	0.83	0.48	15	No	C
3	0.91	0.83	17	No	B
4	0.80	0.67	50	No	C
5	0.90	0.80	89	Yes	A
6	0.61	0.23	17	No	D
7	0.91	0.47	29	Yes	A

<sup>a</sup>Quality classification (A–D) is assigned based on the linearity (L), correlation coefficient (C), Number\_of\_events, and Repeating\_events of clusters. <sup>b</sup>Number of events: the number of events within each cluster. <sup>c</sup>Repeating Events: if the cluster contains any REs.

~60° NNE dipping structure. The seismicity pattern becomes more complex in P4-P4' and P5-P5', as the L/C values decrease to 0.6/0.3 and 0.6/0.01, respectively. These results indicate that it is not possible to interpret the primary structure as a single ~60° NNE dipping zone in the eastern extent of our study area. The results also reveal several secondary structures embedded within in the primary seismicity zone: two vertical structures in P1-P1' (Clusters 1 and 2), an NNE dipping structure in P4-P4' (Cluster 5), a southwest dipping (~15°) structure in P5-P5' (Cluster 6), and a vertical structure in P5-P5' (Cluster 7). We also identify two potential structures in P4-P4' and P5-P5' represented by green dots on Figure 7, which have been identified as clusters in certain clustering runs, but not as stable as Clusters 1 to 7. Five out of seven focal mechanism solutions demonstrate right-lateral strike-slip faulting (Figure 5a). These highly consistent solutions suggest the general deformation below the LRF is right-lateral, or, at least, structures delineated by REs tend to slip with a right-lateral sense. We discuss the implications of these results below.

## 5. Discussion

Unlike plate boundary faults that often have primary slip surfaces definable by seismicity (e.g., Cassidy and Waldhauser, 2003, on the Juan de Fuca plate), forearc crustal faults characterized by slow loading rates can be more difficult to identify using seismicity (Asano & Iwata, 2016; Ferranti et al., 2014). Forearc crustal faults can exhibit relatively low seismicity levels, earthquake focal mechanisms without dominant patterns (Balfour et al., 2011) that may be distributed along fault arrays and fracture networks rather than discrete, planar structures (e.g., Waldhauser & Ellsworth, 2000). In addition, attempts to determine structures based on correlating surficial fault traces with observed seismicity may be difficult if seismogenic clusters deviate from mapped lithological contacts. The identification of seismogenic structures in forearc crust therefore often requires careful treatment, including quantitative and objective clustering methods (e.g., the GMM and RE analysis in this study), as well as investigations of fault kinematics in the field (e.g., Morell et al., 2017), which can collectively reveal previously unknown active structures.

In this study we relocated 1,126 events out of 1,253 CNSN cataloged events between 1992 and 2015, incorporating both catalog and waveform cross-correlation traveltimes differences. Our relocated high-precision crustal earthquake hypocenters (uncertainty ~100 m–200 m) delineate subsurface seismogenic structures in the LRF area. Collectively, these seismicity data define a steeply NNE dipping (~60°) zone that contains numerous potential seismogenic structures, including secondary subvertical structures consisting of REs with highly similar waveforms. This zone of seismicity projects to the surface where fault scarps indicative of recent active slip along the LRF have been mapped (Morell et al., 2017). Focal mechanism solutions of a subset of these earthquakes indicate right-lateral faulting on ~E-W striking structures. Our results provide the first documentation of active terrestrial crustal seismogenic structures in the southern Vancouver Island area, which has significant implications for the Leech River deformation zone structure, regional seismicity, local crustal stress field, and our understanding of forearc crustal faults.

### 5.1. Implications for the Active LRFZ

The LRF was imaged based on the LITHOPROBE reflection profile (Line 2) as a NNE ~45° dipping fault extending to a depth of ~10 km (Figure 4) and has been interpreted as the lithological boundary between schists of the Leech River Complex and basalts of the Metchosin Formation (Clowes et al., 1987). Our relocation results demonstrate that most crustal earthquakes are not colocated with the LITHOPROBE imaged lithological

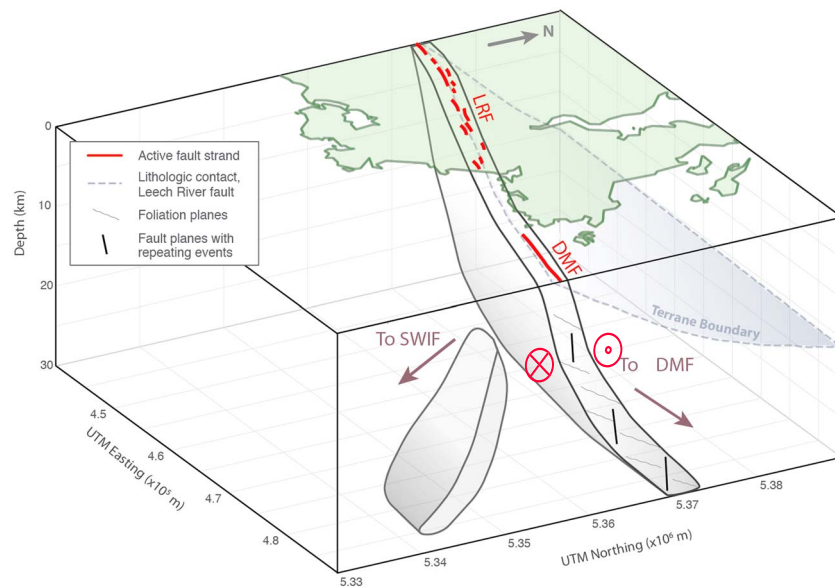


**Figure 8.** Proposed structural interpretation of the seismicity below the Leech River fault zone, showing a steeply dipping fault zone that bifurcates eastward into two fault zones that project into the Devil's Mountain Fault (DMF) and Southern Whidbey Island Fault (SWIF). We interpret the relocated seismicity to fall within a broad deformation zone that contains a network of subvertical fractures and overprints a northeast dipping structural fabric, and which does not reoccupy the lithologic terrane boundary contact between the Crescent and Pacific Rim terranes.

contact but instead occur beneath it (Figure 4), within a region of apparently gently NE dipping ( $<25^\circ$ ) reflectors interpreted to be metamorphosed units of the Cascadia accretionary complex (e.g., Clowes et al., 1987). These data indicate that microseismicity beneath the LRF neither follows the position of the lithologic Leech River Schist-Metchosin basalt contact at depth nor does it appear to parallel the orientation of preexisting structural fabrics in the underlying accretionary units. Similar geologic observations have been made during recent geological surveys along the eastern LRF, which identified topographic scarps and fault planes with strike-slip and reverse slip sense indicators that are not collocated with the lithologic LRF surface trace and dip more steeply than regional foliations (Morell et al., 2017). The combination of this study and these geological observations indicate that if the LRF is active, as our seismicity data suggest, the reactivated fault has not reoccupied the terrane boundary fault imaged in LITHOPROBE profiles. We suggest that the potentially active LRF should instead be interpreted as a  $\sim 10$  km thick, diffusive seismic zone that dips  $\sim 70^\circ$ – $90^\circ$  at the surface and  $\sim 60^\circ$  at depth.

Based on our relocation results, we suggest the subsurface geometry of the LRF seismogenic zone bifurcates along strike from a single northeasterly dipping structure in the west (profiles P1-P1' to P3-P3') into two branches in the east (P4-P4' to P5-P5'). The single northeasterly dipping structure in the west has a finite thickness of 8 to 10 km and dips NNE at  $\sim 60^\circ$ . One of the two branches continues to dip toward the NNE and is potentially linked to the Devil's Mountain Fault (DMF), and another branch dipping toward the SW is potentially linked to the Southern Whidbey Island Fault (SWIF) (Figure 8). We make this conclusion based on the following two observations of the relocated and clustered seismicity. First, the clustering results suggest that it is not possible to determine a single uniformly dipping structure on the eastern extent of our study area within profiles P4-P4' and P5-P5'. Rather, the grouping results from the K-mean method (Lloyd, 1982; see Figure S6) indicate two separate structures within profile P5-P5'. Cluster 7 constitutes the northern structure, and is likely the continuation of the structure observed in P1-P1' to P3-P3'. Cluster 6 represents a secondary structure that branches to the south (Figures 7 and 8). Unlike the GMM method that identifies clusters with high statistical significance, the K-mean method emphasizes the spatial separation between each group. Since P4-P4' is located around where the fault branches, the spatial separation between the two branches is not as clear as in P5-P5'. Second, previous studies show a system of active faults near the LRF extending across the Juan de Fuca Strait into an adjacent fault network in NW Washington (Barrie & Greene, 2015, 2018; Johnson et al., 2001). For example, shallow seismic reflection and sediment core data indicate that the eastern LRF merges along the strike with the western extent of the DMF (which has a

45° to 75°N dip as observed in the upper 2 km) (Barrie & Greene, 2015) and the SWIF (a wide fault zone that consists of both northeast dipping and southwest dipping faults) across the eastern Juan de Fuca Strait (Johnson et al., 2001). The northern branch identified in this study projects to the western extensions of the DMF (Cluster 5, Cluster 7, and the potential structure in P5-P5', Figures 7 and 8). The DMF branch has a NNE dip of ~60° (Johnson et al., 2001), similar to what is observed between P1-P1' and P3-P3'. The potential structures in profile P4-P4' and Cluster 6 project toward the SWIF. The dip of Cluster 6 (~30°) suggests that the SWIF branch has a gentler dip at depth. However, since Cluster 6 has the lowest linearity and it does not contain any REs, it is considered to have the lowest quality among all clusters identified. Therefore, the geometry represented by Cluster 6 may not be well resolved.

## 5.2. Secondary Structures

Based on the GMM and RE methods, we are able to quantitatively and objectively identify seven vertical structures within the broader LRFZ. We interpret these vertical structures as secondary structures developed within the LRFZ. While relocated seismicity broadly defines a ~60° NE dipping fault zone structure, focal mechanism solutions of repeating earthquakes suggest the fault zone accommodates right-lateral strike-slip motion at depth along steeply dipping, approximately E-W striking planes. We suggest that the discrepancy between the moderate dip of the proposed major structure and the vertical dip of identified smaller structures is a result of the combined development of new subvertical strike-slip fault segments and the reactivation of preexisting north dipping foliation in the Cascadia accretionary complex (Figure 8). In this interpretation, foliation planes may transfer strain between adjacent subvertical fractures, with an overall geometry similar to the en echelon fracture arrays that develop during the stages of initial fault growth and linkage (e.g., Lunn et al., 2008). We further suggest that our relocated data may highlight a fracture mesh developed within a strike-slip system. The concept of meshes of interconnecting shear and extensional fractures were first proposed by Hill (1977) to describe earthquakes swarms in magmatic settings. Assuming that the orientations of  $\sigma_1$  and  $\sigma_3$  are subhorizontal with  $\sigma_1$  parallel to fault strike and  $\sigma_3$  perpendicular to it, the secondary structures may play a role in forming a mesh fracture in a strike-slip system, similar to what has been observed in the 2008 Mogul earthquake swarm in Nevada (Ruhl et al., 2016), which identified a network of many short en echelon strike-slip faults within a fault-fracture mesh. We propose, based on our earthquake relocation and clustering results as well as geological fieldwork (Morell et al., 2017), that the LRF deformation zone consists of a steeply dipping fracture network that likely overprints the preexisting, moderately north-east dipping foliation/bedding structural fabric developed within accreted units in the Cascadia forearc (Figure 4). The existing data indicates a set of distinct, subvertical seismogenic structures within a 10 km thick seismic zone. We interpret these structures to be part of a fracture network instead of discrete faults. This interpretation would imply that only a subset of the fractures currently hosts microseismicity in the current crustal stress field and under the present fluid pressure conditions. There are also similar geologic observations along the surface trace of the LRFZ (Morell et al., 2017), where brittle faults appear to define a network of fractures subparallel to the LRFZ trace.

## 5.3. Regional Seismicity Implications

In addition to the identification of terrestrial crustal fault structures, we can also infer information about the regional seismicity on southern Vancouver Island from the relocated events. As shown in Figure 4, our relocated earthquakes define two groups separated by a ~10 km seismicity gap. This gap coincides with a seismically high reflection zone first imaged in the LITHOPROBE project (Clowes et al., 1987) and later identified to be part of a broad (~10 km wide) high reflection zone at the top of the subduction slab in northern Cascadia (Nedimovic et al., 2003). Low seismic wave velocity and high electronic conductivity have been reported for the high reflection band (Hyndman, 1998) and have been interpreted to reflect weak materials incapable of accumulating stress that could be released in dynamic events (Calvert, 2004). This low-velocity zone has also been suggested to be the source region for nonvolcanic tremors on Vancouver Island (Kao et al., 2005). Some studies suggest this high reflection band lies directly on top of the subducted oceanic slab (Clowes et al., 1987; Nedimovic et al., 2003), while others indicate it is located several kilometers above the top of the oceanic slab (Cassidy & Waldhauser, 2003; Hyndman, 1998; Kao et al., 2005). More recently, Bostock (2013) proposed a new model to reconcile the previously conflicting interpretations in which the high-reflection zone (also termed low-velocity zone, LVZ) is essentially composed of hydrated pillow basalts and sheeted dikes of an oceanic crustal layer. Bostock (2013) suggests that the widely detected LVZ in major

subduction zones is a result of overpressurization of the upper oceanic crust confined between a subduction “seal” above and a low porosity gabbro layer below. Although our relocation results do support the presence of such a seismicity gap, it is hard to tell which model is favorable based on our study. We also observe that most of the relocated seismicity is in the accretionary units instead of the overlying Metchosin Formation basalts (Figure 4). This concentration of seismicity suggests that the identified fault zone is reactivated in the underlying accretionary units. Crustal earthquakes are generated at considerable depths within the crust ( $\sim 15$ – $25$  km), as shown in the depth profiles in Figure 7. This phenomenon of deep brittle faulting, which is widespread in global forearc areas, for example, SW Japan (Salah & Zhao, 2003), may be due to an unusually low heat flow beneath the forearc area as the subduction of the oceanic plate can be considered as a heat sink and dominates the local thermal structure (Dragert et al., 1994). For example, heat flow measured on the southern Vancouver Island area reaches as low as  $33 \text{ mW m}^{-2}$  (Lewis et al., 1988), which is significantly lower than southern California heat flow measurements of  $70 \text{ mW m}^{-2}$  or above (Bryant & Jones, 1992).

In map view, most of the earthquakes near the LRF are clustered along the Leechtown-Colwood (east) segment while the Sombrio-Leechtown (west) segment appears seismically quiescent. We suggest the following three possibilities for the apparent seismic activity contrast. First, seismic studies from LITHOPROBE profiles offshore reveal that the high reflection zone is a regionally extensive, eastward dipping structure which occurs at depths of  $\sim 15$  km beneath the western part of southern Vancouver Island to 30 km in the eastern part (Nedimovic et al., 2003). We speculate that the presence of the shallower aseismic reflectors within the high reflectivity zone beneath the western segment may inhibit crustal seismicity at this depth. By contrast, crustal seismicity is more abundant on the eastern segment of the LRF, where the high reflection zone exists at depths greater than  $\sim 30$  km. Second, the change in the strike orientation of the LRF relative to the local stress field from west to east may also contribute to the seismicity difference. Previous stress inversion studies based on focal mechanism solutions within the crust of the overriding plate suggest the orientation of the local maximum horizontal compressive stress direction  $S_{Hmax}$  varies from the subduction trench to the volcanic arc across southern Vancouver Island (Balfour et al., 2011); the orientation of  $S_{Hmax}$  near the LRF is much more oblique ( $\sim 80^\circ$ ) to the Sombrio-Leechtown (west) segment than the orientation ( $\sim 10^\circ$ ) to the Leechtown-Colwood (east) segment (Figure 1b). Therefore, a steeply dipping LRF fault-parallel shear zone could promote strike-slip kinematics in the east, while fault-normal clamping could inhibit activity in the west. Observations of topographic scarps with morphologies characteristic of strike-slip systems along the eastern LRF segment support this interpretation (Morell et al., 2017). However, we cannot exclude the possibility that intrinsically low fault strength can also lead to seismic failure even in a nonoptimally oriented stress fields (e.g., Hardebeck & Michael, 2004). We note that neither the low forearc heat flow nor the dipping structure of the aseismic reflectors is sufficient to explain the lack of shallow seismicity above  $\sim 10$  km along the eastern segment. Future studies on high-resolution local seismic velocity structure and near-fault continuous geodetic monitoring may reveal if fault loading and/or the architecture of the upper  $\sim 10$  km of the crust significantly varies from conditions at depth.

## 6. Conclusions

Microseismicity relocations and cluster identifications delineate seismogenic structures near the LRF on southern Vancouver Island within the Cascadia subduction zone forearc. We use HypoDD double-difference method to relocate 1,126 out of 1,253 CNSN cataloged earthquakes between 1992 and 2015, with a focus on events in the upper 30 km in the forearc crust near the LRF zone. To a first order, the crustal seismicity highlights a wide ( $\sim 10$  km wide) steeply NNE dipping structure beneath the Leechtown-Colwood segment, which clearly deviates from the LITHOPROBE imaged lithological contact between the Leech River Complex and the Metchosin Formation. We further apply independent clustering techniques to identify seismically active structures of both broad ( $\sim 10$  km wide) and fine (1–2 km wide) scales and their variation along the LRF. Our results suggest the broad LRF zone bifurcates into two structures offshore to the east, with the north branch continuing to dip NNE, possibly connected to the DMF and the south branch possibly linked to the SWIF. Secondary, more discrete structures are defined as vertically dipping fractures accommodating right-lateral slip and may reflect the existence of preexisting foliations at depth. We propose that the LRF is a deformation zone with a steeply dipping fracture network overprinting a moderately dipping structural fabric, resulting in a fracture mesh developed in a strike-slip system. Our results provide the first confirmation of terrestrial crustal faults on southern Vancouver Island using microseismicity and suggest that slowly



slipping active crustal faults may result in geometric distributions of microseismicity that differ from larger, more rapidly slipping plate boundary faults, especially in regions with a preexisting structural fabric.

# Acknowledgments

We would like to thank Natalie Balfour and Taimi Mulder for providing valuable focal mechanism solutions, and Hongyu Yu for valuable discussions on using HypoDD. We also thank Christine Ruhl and an anonymous reviewer for their constructive comments that helped to improve the presentation of this manuscript. This work is supported by the Fonds de recherche Nature et technologies Québec, Projet de recherche en équipe(191259) to Y. Liu at McGill, a National Science Foundation EAR IRFP (1349586) to C. Regalla at Boston U., and an NSERC Discovery Grant (RGPIN-2014-04260) to K. Morell at U.Vic. The original catalog earthquake hypocenters were downloaded from the Canadian National Seismograph Network (CNSN) (<http://www.earthquakescanada.nrcan.gc.ca/stndon/NEDB-BNDS/bull-en.php>). Catalog traveltimes were obtained via e-mail contact with CNSN staff.

# References

- Asano, K., & Iwata, T. (2016). Source rupture processes of the foreshock and mainshock in the 2016 Kumamoto earthquake sequence estimated from the kinematic waveform inversion of strong motion data. *Earth, Planets and Space*, 68(1), 147. <https://doi.org/10.1186/s40623-016-0519-9>
- Balfour, N. J., Cassidy, J. F., Dosso, S. E., & Mazzotti, S. (2011). Mapping crustal stress and strain in southwest British Columbia. *Journal of Geophysical Research*, 116, B03314. <https://doi.org/10.1029/2010JB008003>
- Balfour, N. J., Cassidy, J. F., & Dosso, S. E. (2012). Identifying active structures using Double-Difference earthquake relocations in Southwest British Columbia and the San Juan Islands, Washington. *Bulletin of the Seismological Society of America*, 102(2), 639–649. <https://doi.org/10.1785/0120110056>
- Barrie, J. V., & Greene, H. G. (2015). Active faulting in the northern Juan de Fuca Strait implications for Victoria, British Columbia, Geo. Surv. Can., Current Research 2015-6 (pp. 10). <https://doi.org/10.4095/296564>
- Barrie, J. V., & Greene, H. G. (2018). The Devils Mountain Fault zone: An active Cascadia upper plate zone of deformation, Pacific Northwest of North America. *Sedimentary Geology*, 364, 228–241. <https://doi.org/10.1016/j.sedgeo.2017.12.018>
- Bostock, M. G. (2013). The Moho in subduction zones. *Tectonophysics*, 609, 547–557. <https://doi.org/10.1016/j.tecto.2012.07.007>
- Bryant, A. S., & Jones, L. M. (1992). Anomalous deep crustal earthquakes in the Ventura Basin, Southern California. *Journal of Geophysical Research*, 97, 437–447. <https://doi.org/10.1029/91JB02286>
- Calvert, A. J. (2004). Seismic reflection imaging of two megathrust zones in the northern Cascadia subduction zone. *Nature*, 428(6979), 163–167. <https://doi.org/10.1038/nature02372>
- Cassidy, J. F., Rogers, G. C., & Waldhauser, F. (2000). Characterization of active faulting beneath the strait of Georgia, British Columbia. *Bulletin of the Seismological Society of America*, 90(5), 1188–1199. <https://doi.org/10.1785/0120000044>
- Cassidy, J. F., & Waldhauser, F. (2003). Evidence for both crustal and mantle earthquakes in the subducting Juan de Fuca plate. *Geophysical Research Letters*, 30(2), 1095. <https://doi.org/10.1029/2002GL015111>
- Clowes, R. M., Brandon, M. T., Green, A. G., Yorath, C. J., Brown, A. S., Kanasweich, E. R., & Spencer, C. (1987). LITHOPROBE-southern Vancouver Island: Cenozoic subduction complex imaged by deep seismic reflections. *Canadian Journal of Earth Sciences*, 24(1), 31–51. <https://doi.org/10.1139/e87-004>
- Dragert, H., Hyndman, R. D., Rogers, G. C., & Wang, K. (1994). Current deformation and the width of the seismogenic zone of the northern Cascadia subduction thrust. *Journal of Geophysical Research*, 99, 653–668. <https://doi.org/10.1029/93JB02516>
- Ferranti, L., Palano, M., Cannavò, F., Mazzella, M. E., Oldow, J. S., Gueguen, E., et al. (2014). Rates and geodetic deformation across active faults in southern Italy. *Tectonophysics*, 621, 101–122. <https://doi.org/10.1016/j.tecto.2014.02.007>
- Fisher, M. A., Brocher, T. M., Hyndman, R. D., Trehu, A. M., Weaver, C. S., Creager, K. C., et al. (1999). Seismic survey probes urban earthquake hazards in Pacific Northwest. *Eos, Transactions American Geophysical Union*, 80(2), 13–17. <https://doi.org/10.1029/99EO00011>
- Gardonio, B., Marsan, D., Lengline, O., Enescu, B., Bouchon, M., & Got, J. (2015). Changes in seismicity and stress loading on subduction faults in the Kanto region, Japan, 2011–2014. *Journal of Geophysical Research: Solid Earth*, 120, 2616–2626. <https://doi.org/10.1002/2014JB011798>
- Hardebeck, J. L., & Michael, A. J. (2004). Stress orientations at intermediate angles to the San Andreas Fault, California. *Journal of Geophysical Research*, 109, B11303. <https://doi.org/10.1029/2004JB003239>
- Hardebeck, J. L., & Shearer, P. M. (2003). Using S/P amplitude ratios to constrain the focal mechanism of small earthquakes. *Bulletin of the Seismological Society of America*, 93(6), 2434–2444. <https://doi.org/10.1785/0120020236>
- Hauksson, E., & Shearer, P. (2005). Southern California hypocenter relocation with waveform cross-correlation. Part 1: Results using the double-difference method. *Bulletin of the Seismological Society of America*, 95(3), 896–903. <https://doi.org/10.1785/0120040167>
- Hill, D. P. (1977). A model for earthquake swarms. *Journal of Geophysical Research*, 82, 1347–1352. <https://doi.org/10.1029/JB082i008p01347>
- Hyndman, R. D. (1998). Dipping seismic reflectors, electrically conductive zones, and trapped water in the crust over a subducting plate. *Journal of Geophysical Research*, 93, 13,391–13,405.
- Johnson, S. Y., Dadisman, S. V., Childs, J. R., & Stanley, W. D. (1999). Active tectonics of the Seattle fault and central Puget Sound, Washington—Implications for earthquake hazards. *GSA Bulletin*, 111(7), 1042–1053. [https://doi.org/10.1130/00167606\(1999\)111%3C1042:ATOTSF%3E2.3.CO;2](https://doi.org/10.1130/00167606(1999)111%3C1042:ATOTSF%3E2.3.CO;2)
- Johnson, S. Y., Dadisman, S. V., Mosher, D. C., Blakely, R. J., & Childs, J. R. (2001). Active tectonics of the Devils Mountain Fault and related structures, Northern Puget Lowland and eastern Strait of Juan de Fuca region, Pacific Northwest, U.S. Geological Survey Professions Paper, 1643.
- Kao, H., Shan, S. J., Dragert, H., Rogers, G., Cassidy, J. F., & Ramachandran, K. (2005). A wide depth distribution of seismic tremors along the northern Cascadia margin. *Nature*, 436(7052), 841–844. <https://doi.org/10.1038/nature03903>
- Kimura, H., Kasahara, K., Igarashi, T., & Hirata, N. (2006). Repeating earthquake activities associated with the Philippine Sea plate subduction in the Kanto district, central Japan: A new plate configuration revealed by interplate aseismic slips. *Tectonophysics*, 417, 101–118. <https://doi.org/10.1016/j.tecto.2005.06.013>
- Lewis, T. J., Bentkowski, W. H., Davis, E. E., & Hyndman, R. D. (1988). Subduction of the Juan de Fuca plate: Thermal consequences. *Journal of Geophysical Research*, 93, 15,207–15,225.
- Lloyd, S. P. (1982). Least squares quantization in PCM. *IEEE Transactions on Information Theory*, 28(2), 129–137. <https://doi.org/10.1109/TIT.1982.1056489>
- Lunn, R. J., Willson, J. P., Shipton, Z. K., & Moir, H. (2008). Simulating brittle fault growth from linkage of pre-existing structures. *Journal of Geophysical Research*, 113, B07403. <https://doi.org/10.1029/2007JB005388>
- MacLeod, N. S., Tiffin, D. L., Snavely, P. D., & Currie, R. G. (1977). Geologic interpretation of magnetic and gravity anomalies in the Strait of Juan de Fuca, U.S.–Canada. *Canadian Journal of Earth Sciences*, 14(2), 223–238. <https://doi.org/10.1139/e77-024>
- Massey, N. W. D., MacIntyre, D. G., Desjardins, P. J., & Cooney, R. T. (2005). Digital map of British Columbia: Whole Province, B.C. Ministry of Energy and Mines, GeoFile 2005 1.
- McCaffrey, R., Qamar, A., King, R., Wells, R., Khazaradze, G., Williams, C., et al. (2007). Fault locking, block rotation and crustal deformation in the Pacific northwest. *Geophysical Journal International*, 169(3), 1315–1340. <https://doi.org/10.1111/j.1365-246X.2007.03371.x>

- McLachlan, G., & Peel, D. (2000). *General introduction, in finite mixture models* (pp. 1–39). Hoboken, NJ: John Wiley. <https://doi.org/10.1002/0471721182.ch1>
- Morell, K. D., Regalla, C., Leonard, L. J., Amos, C., & Levson, V. (2017). Quaternary rupture of a crustal fault beneath Victoria, British Columbia, Canada. *GSA Today*, 27, 4–10. <https://doi.org/10.1130/GSATG291A.1>
- Mosher, D. C., Cassidy, J. F., Lowe, C., Mi, Y., Hyndman, R. D., Rogers, G. C., & Fisher, M. (2000). Neotectonics in the strait of Georgia: First tentative correlation of seismicity with shallow geological structure in southwestern British Columbia, Current research, P.A22.
- Nedimovic, M. R., Hyndman, R. D., Ramachandran, K., & Spence, G. D. (2003). Reflection signature of seismic and aseismic slip on the northern Cascadia subduction interface. *Nature*, 424(6947), 416–420. <https://doi.org/10.1038/nature01840>
- Paige, C. C., & Saunders, M. A. (1982). LSQR: An algorithm for sparse linear equations and sparse least squares. *ACM Transactions on Mathematical Software*, 8(1), 43–71. <https://doi.org/10.1145/355984.355989>
- Ramachandran, K., Hyndman, R. D., & Brocher, T. M. (2006). Regional *P*-wave velocity structure of the northern Cascadia subduction zone. *Journal of Geophysical Research*, 111, B12301. <https://doi.org/10.1029/2005JB004108>
- Rogers, G. C. (1994). Earthquakes in the Vancouver Area. *Geological Survey of Canada Bulletin*, 481, 221–229.
- Ruhl, C. J., Abercrombie, R. E., Smith, K. D., & Zaliapin, I. (2016). Complex spatiotemporal evolution of the 2008 Mw 4.9 earthquake swarm (Reno, Nevada): Interplay of fluid and faulting. *Journal of Geophysical Research: Solid Earth*, 121, 8196–8216. <https://doi.org/10.1002/2016JB013399>
- Rushmore, M. E., & Cowan, D. S. (1985). Jurassic-Cretaceous rock units along the southern edge of the Wrangellia terrane on Vancouver Island. *Canadian Journal of Earth Sciences*, 22(8), 1223–1232. <https://doi.org/10.1139/e85-124>
- Salah, M., & Zhao, D. (2003). 3-D seismic structure of Kii Peninsula in southwest Japan: Evidence for slab dehydration in the forearc. *Tectonophysics*, 364(3–4), 191–213. [https://doi.org/10.1016/S0040-1951\(03\)00059-3](https://doi.org/10.1016/S0040-1951(03)00059-3)
- Sarigiotes, C. D., Hadjileontiadis, L. J., Rekanos, I. T., & Panas, S. M. (2004). Automatic P phase picking using maximum kurtosis and -statistics criteria. *IEEE Geoscience and Remote Sensing Letters*, 1(3). <https://doi.org/10.1109/LGRS.2004.828915>
- Sherrod, B., Blakely, R., Weaver, C., Kelsey, H., Barnett, E., Liberty, L., et al. (2008). Finding concealed active faults: Extending the southern Whidbey Island fault across the Puget Lowland, Washington. *Journal of Geophysical Research*, 113, B05313. <https://doi.org/10.1029/2007JB005060>
- Sherrod, B. L., Blakely, R. J., Lasher, J. P., Lamb, A., Mahan, S. A., Foit, F. F., & Barnett, E. A. (2016). Active faulting on the Wallula fault zone within the Olympic-Wallowa lineament, Washington State, USA. *GSA Bulletin*, 128(11–12), 1636–1659. <https://doi.org/10.1130/B31359.1>
- Tsutsumi, H., & Okada, A. (1996). Segmentation and Holocene surface faulting on the Median Tectonic Line, Southwest Japan. *Journal of Geophysical Research*, 101, 5855–5871. <https://doi.org/10.1029/95JB01913>
- Waldhauser, F., & Ellsworth, W. L. (2000). A double-difference earthquake location algorithm: Method and application to the northern Hayward fault California. *Bulletin of the Seismological Society of America*, 90(6), 1353–1368. <https://doi.org/10.1785/0120000006>
- Waldhauser, F., & Schaff, D. P. (2008). Large-scale relocation of two decades of Northern California seismicity using cross-correlation and double-difference methods. *Journal of Geophysical Research*, 113, B08311. <https://doi.org/10.1029/2007JB005479>
- Yu, H., Liu, Y., Harrington, R. M., & Lamontagne, M. (2016). Seismicity along St. Lawrence Paleorift faults overprinted by a meteorite impact structure in Charlevoix, Québec, Eastern Canada. *Bulletin of the Seismological Society of America*, 106(6), 2663–2673. <https://doi.org/10.1785/0120160036>
- Zaleski, M. P. (2014). Earthquake loss estimates, Greater Victoria, British Columbia, MSc. thesis, Simon Fraser University, Burnaby, B. C., Canada. <https://doi.org/10.1155/2014/720507>
- Zaliapin, I., & Ben-Zion, Y. (2013). Earthquake clusters in southern California I: Identification and stability. *Journal of Geophysical Research: Solid Earth*, 118, 2847–2864. <https://doi.org/10.1002/jgrb.50179>